QED effects on Kerr black hole shadows immersed in uniform magnetic fields

Zhen Zhong,[1] Zezhou Hu,[2] Haopeng Yan,[3] Minyong Guo,[1,*] and Bin Chen[2,3,4]

[1]*Department of Physics, Beijing Normal University, Beijing 100875, People's Republic of China*
[2]*School of Physics, Peking University, No.5 Yiheyuan Rd, Beijing 100871, People's Republic of China*
[3]*Center for High Energy Physics, Peking University, No.5 Yiheyuan Rd, Beijing 100871, People's Republic of China*
[4]*Collaborative Innovation Center of Quantum Matter, No.5 Yiheyuan Rd, Beijing 100871, People's Republic of China*

(Received 23 August 2021; accepted 19 October 2021; published 11 November 2021)

In this work, taking the QED effect into account, we investigate the shadows of the Kerr black holes immersed in uniform magnetic fields through the numerical backward ray-tracing method. We introduce a dimensionless parameter Λ to characterize the strength of magnetic fields and study the influence of magnetic fields on the Kerr black hole shadows for various spins of the black holes and inclination angles of the observers. In particular, we find that the photon "hairs" appear near the left edge of the shadow in the presence of magnetic fields. The photon hairs may be served as a signature of the magnetic fields. We notice that the photon hairs become more evident when the strength of magnetic fields or the spin of the black hole becomes larger. In addition, we study the deformation of the shadows by bringing in quantitative parameters that can describe the position and shape of the shadow edge.

DOI: 10.1103/PhysRevD.104.104028

I. INTRODUCTION

Black holes play a very important role in understanding the nature of gravity and spacetimes. As technology improves, people are now able to hear black holes through LIGO and Virgo [1], and to see black holes with the help of the Event Horizon Telescope (EHT) [2]. In particular, the image of the supermassive black hole at the center of M87 galaxy has the up-down asymmetry, that is, a prominent rotationally-symmetric mode, which suggests that the black hole has to be spinning. Up to now, the best model mimicking a real rotating black hole in our Universe is generally considered to be the Kerr spacetime. With the confidence and motivation given by the observational images of black holes, theoretical research has been widely carried out in recently years. Inspired by the pioneer works [3,4], people have studied the observational signatures of supermassive objects on many aspects including the shadows [5–17], the images of companion stars [18–21], the photon rings [22–29], etc., [30–42].

Recently, almost two years after the first picture was released in 2019, the EHT Collaboration published the polarized image of M87*, from which we can clearly see that there is an extra twisting polarization pattern for the bright ring compared to the first image [43]. Since in magnetic fields the polarization of photons would rotate as in Faraday effects, it has been argued that the polarized image should be caused by the synchrotron radiation of innermost charged particles of the accretion disk moving in a magnetic field. Thus the polarized image of M87* indicates that, around the black hole, there must exist a strong magnetic field [44] and the polarization structure depends on both the spacetime and the magnetic fields around a black hole.

As we know, classically the magnetic fields do not affect the trajectories of photons, so that black hole shadows formed by countless light traces are only directly determined by the spacetime structure. However, in practice there are a few indirect ways through which the magnetic fields can affect the motion of the photons. One obvious way is that if the magnetic field is strong enough, its reaction to the spacetime should be taken seriously such that the background metric would be changed. Consequently the motions of the photons get modified as well. Along this line, in [45,46], the authors have investigated the Schwarzschild and the Kerr black hole shadows in the Melvin magnetic field. The advantage of this analysis is that the influence of the magnetic field on the black hole shadows can be easily studied, whereas, the spacetime in a Melvin magnetic field is not asymptotically flat any more.

In this paper, we study the influence of the magnetic fields on the Kerr black hole shadow in an alternative way, which has been discussed in our previous paper [47] in the context

*Corresponding author.
minyongguo@bnu.edu.cn.

of a static black hole. As we know, astronomical black holes in reality are always expected to be rotating and the Kerr black hole solution has been considered as the most competitive model to mimic a real black hole in the Universe. Thus, it is necessary to generalize our previous work [47] to the Kerr black holes. In addition, compared to the Schwarzschild black holes, the shadows of the Kerr black holes have much richer structures. Therefore, it is also interesting to see how magnetic fields affect the shadows when the spin of a black hole becomes significant. Moreover, as mentioned above, we focus our attention on the situation where the magnetic fields are not strong enough to modify the geometry of background spacetime; instead, our strategy is to take the quantum electrodynamics (QED) effect on the photons into account. In this case, by including the birefringence [48,49] induced by the QED effect, the motions of massless particles would deviate from the geodesics if the black hole is immersed in a magnetic field, and now we are able to investigate the effects of magnetic fields on the Kerr black hole shadows. In this work, we pay attention to the Kerr black hole with a uniform magnetic field outside the horizon. Using the numerical backward ray-tracing method, we investigate the Kerr black hole shadows under the influence of the magnetic field. In particular, we show that with increasing magnetic fields or increasing spin, the photon hairs appearing near the left edge of the shadow, which could be taken as a signature of the magnetic field, become more evident. Furthermore, we introduce six parameters to characterize the edges of the shadows, and quantitatively calculate the deformations of the shadow edges affected by the uniform magnetic field.

The remaining parts of this paper is organized as follows. In Sec. II we give a brief review on the dispersion relations induced by the QED effect and derive the equations of motion. In Sec. III we study the shadows of Kerr black holes immersed in the uniform magnetic fields in detail. In Sec. IV we summarize our results. In this work, we have set the fundamental constants c, G, the vacuum permittivity ε_0, and the mass of the black hole M to unity, and we will work in the convention $(-,+,+,+)$.

II. DISPERSION RELATIONS AND EQUATIONS OF MOTION

As shown in our previous paper [47], the action involving the electromagnetic gauge potential minimally coupled to gravity takes the form

$$I = \int d^4x\sqrt{-g}\left(\frac{1}{16\pi}R + L_{\text{eff}}\right), \tag{2.1}$$

where L_{eff} is the Euler-Heisenberg effective Lagrangian for the electromagnetic field which can describe the one-loop vacuum polarization and reads

$$L_{\text{eff}} = -\frac{1}{4}F_{\mu\nu}F^{\mu\nu} - \frac{\mu}{2}\left[\frac{5}{4}(F_{\mu\nu}F^{\mu\nu})^2 - \frac{7}{2}F_{\mu\nu}F_{\sigma\tau}F^{\mu\sigma}F^{\nu\tau}\right], \tag{2.2}$$

and the coupling constant is defined as

$$\mu = \frac{\hbar e^4}{360\pi^2 m_e^4}, \tag{2.3}$$

where m_e is the electron mass and e denotes the charge of the electron. After straightforward and standard calculations, one can obtain the dispersion relation and the effective metric given as follows:

$$0 = p_\alpha p_\beta(g^{\alpha\beta} + X_{\alpha\beta}), \tag{2.4}$$

$$G_{\alpha\beta} = g_{\alpha\beta} + X_{\alpha\beta}, \tag{2.5}$$

where p_α is the momentum of the photon, and a new tensor $X_{\alpha\beta} \equiv \lambda F^\mu{}_\alpha F_{\mu\beta}$ was introduced for simplicity with $\lambda = -8\mu$ or -14μ giving two different polarizations of the photons.

With the above effective metric, one can define the dual vector q_μ as $G_{\mu\nu}p^\nu$. Then the conjugate variables (x^μ, q_μ) would satisfy the canonical equations as follows:

$$\dot{q}_\mu = -\frac{\partial H}{\partial x^\mu}, \qquad \dot{x}^\mu = \frac{\partial H}{\partial q_\mu}, \tag{2.6}$$

$$H = H(q_\mu, x^\mu) = G^{\mu\nu}(x)q_\mu q_\nu. \tag{2.7}$$

We want to stress that here we use $G^{\mu\nu}$ to denote the inverse matrix of $G_{\mu\nu}$, other than $G^{\mu\nu}(x) = g^{\mu\rho}g^{\nu\sigma}G_{\rho\sigma}$. That is, we have $G^{\mu\nu}G_{\nu\sigma} \equiv \delta^\mu_\sigma$.

III. SHADOW OF KERR BLACK HOLES IN THE UNIFORM MAGNETIC FIELD

In this section we focus on a specific case that the Kerr black hole is immersed in the uniform magnetic field. The uniform magnetic field we are interested in is assumed to be not very strong, so that we are allowed to ignore the back-reaction from the magnetic field to the Kerr metric. The Kerr metric in the Boyer-Lindquist coordinate takes the form

$$g_{\mu\nu}dx^\mu dx^\nu = -\left(1 - \frac{2r}{\Sigma}\right)dt^2 + \frac{\Sigma}{\Delta}dr^2 + \Sigma d\theta^2 + \frac{1}{\Sigma}[(r^2+a^2)^2 - \Delta a^2\sin^2\theta]\sin^2\theta d\phi^2 - \frac{4ar}{\Sigma}\sin^2\theta dt d\phi, \tag{3.1}$$

where

$$\Delta = r^2 - 2r + a^2, \qquad \Sigma = r^2 + a^2\cos^2\theta. \tag{3.2}$$

We consider a stationary uniform magnetic field, which is independent of the coordinates t and ϕ. The gauge field A_μ can be solved from the source-free Maxwell equations, that is, $\nabla_\mu F^{\mu\nu} = 0$. An elegant procedure to find the solutions was first presented in [50]. And, the nonzero components of the gauge field A_μ read

$$A_t = -\frac{aBr}{\Sigma}\sin^2\theta - 2aB\left(\frac{1}{2} - \frac{r}{\Sigma}\right),$$
$$A_\phi = \frac{B}{\Sigma}[(r^2+a^2)^2 - \Delta a^2\sin^2\theta]\sin^2\theta - \frac{2a^2Br}{\Sigma}\sin^2\theta. \tag{3.3}$$

Here in our notation we have set the mass of the black hole to be unity, hence a can be directly treated as the angular momentum of the Kerr black hole.

Then from Eq. (2.5), we can obtain the effective metric. However, the explicit forms of the components of $G_{\mu\nu}$ are too complicated to be written down here, and we leave them to Appendix. Based on the effective metric, we would like to determine the motions of the photons using the Hamilton-Jacobi equation

$$G^{\mu\nu}(x)\frac{\partial S}{\partial x^\mu}\frac{\partial S}{\partial x^\nu} = 0. \tag{3.4}$$

After some calculations, one can easily see that the system is nonintegrable due to the lack of the symmetry associated with the Carter constant. Thus in order to figure out the shadow structure of the effective black hole, we have to turn to the numerical backward ray-tracing method which has been introduced in detail in the paper [47]. In the present work, we would not like to bore the readers with the details of the numerical backward ray-tracing method. Instead, let us review the essential points of the method.

Roughly speaking, we use spherical illumination to obtain the image of the black hole in the backward ray-tracing method. We place a ball-like extended source at infinity to illuminate the system and the black hole and the camera are inside the ball-like source. Furthermore, we divide the ball into grids with a network made of latitudinal and longitudinal lines. Each grid is assigned a color standing for four symmetric parts of the celestial sphere. In addition, we employ the fish-eye camera model to photograph the Kerr black hole. The local rest frame of the camera we use is the usual zero-angular-momentum-observer (ZAMO) tetrad which takes the following form,

$$e_0 = \frac{g_{\phi\phi}\partial_t - g_{\phi t}\partial_\phi}{\sqrt{g_{\phi\phi}(g_{\phi t}^2 - g_{\phi\phi}g_{tt})}}, \tag{3.5}$$

$$e_1 = -\frac{\partial_r}{\sqrt{g_{rr}}}, \tag{3.6}$$

$$e_2 = \frac{\partial_\theta}{\sqrt{g_{\theta\theta}}}, \tag{3.7}$$

$$e_3 = -\frac{\partial_\phi}{\sqrt{g_{\phi\phi}}}. \tag{3.8}$$

In the ZAMO frame, the electromagnetic field in the background can be written as

$$X_{(a)(b)} = X_{\mu\nu}e^\mu_{(a)}e^\nu_{(b)}. \tag{3.9}$$

On the other hand, we use the stereographic projection to build a connection between the celestial sphere to the screen of our camera, and the celestial coordinates Θ and Φ can be understood from Fig. 1. Thus, in the ZAMO frame, the 4-momentum of a photon can be expressed as

$$p = -\kappa e_{(0)} + |OP|(\cos\Theta e_{(1)} + \sin\Theta\cos\Psi e_{(2)} + \sin\Theta\sin\Psi e_{(3)}). \tag{3.10}$$

Note that the photons travel along the null geodesics with respect to the effective metric. That is, from Eq. (2.4) one has

$$-\kappa^2 + |OP|^2 + \kappa^2 c_1 + \kappa|OP|c_2 + |OP|^2 c_3 = 0, \tag{3.11}$$

where combining with Eqs. (3.9) and (3.10), the factors c_i $(i = 1, 2, 3)$ read

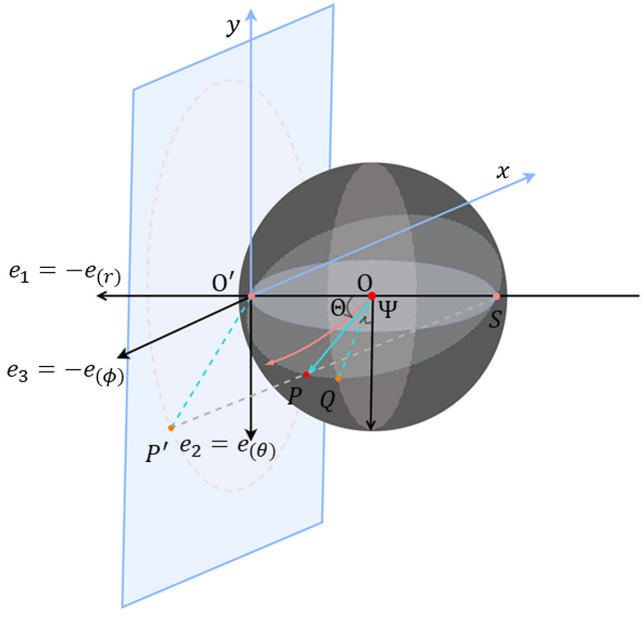

FIG. 1. The ZAMO tetrad of the camera and the celestial coordinates Θ and Φ based on the stereographic projection. This diagram has been shown in Fig. 11 of our previous work [47].

$$c_1 = \gamma\left(X_{tt} + \frac{g_{t\phi}^2}{g_{\phi\phi}^2}X_{\phi\phi} - 2\frac{g_{t\phi}}{g_{\phi\phi}}X_{t\phi}\right), \tag{3.12}$$

$$c_2 = 2\sqrt{\gamma}\left(\frac{\cos\Theta}{\sqrt{g_{rr}}}\zeta_r - \frac{\sin\Theta\cos\Psi}{\sqrt{g_{\theta\theta}}}\zeta_\theta + \frac{\sin\Theta\sin\Psi}{\sqrt{g_{\phi\phi}}}\zeta_\phi\right), \tag{3.13}$$

$$\begin{aligned} c_3 = {} & \frac{X_{rr}}{g_{rr}}\cos^2\Theta - \frac{2X_{r\theta}}{\sqrt{g_{rr}g_{\theta\theta}}}\cos\Theta\sin\Theta\cos\Psi \\ & + \frac{X_{\theta\theta}}{g_{\theta\theta}}\sin^2\Theta\cos^2\Psi + \frac{2X_{r\phi}}{\sqrt{g_{rr}g_{\phi\phi}}}\cos\Theta\sin\Theta\sin\Psi \\ & - \frac{2X_{\theta\phi}}{\sqrt{g_{\theta\theta}g_{\phi\phi}}}\sin^2\Theta\sin\Psi\cos\Psi + \frac{X_{\phi\phi}}{g_{\phi\phi}}\sin^2\Theta\sin^2\Psi, \end{aligned} \tag{3.14}$$

in which we have also introduced several new parameters, including

$$\gamma = \frac{g_{\phi\phi}}{g_{t\phi}^2 - g_{tt}g_{\phi\phi}} > 0, \tag{3.15}$$

outside the horizon of the Kerr black hole, and

$$\zeta_i = X_{ti} - \frac{g_{t\phi}}{g_{\phi\phi}}X_{i\phi}, \qquad i = r, \theta, \phi, \tag{3.16}$$

which appeared in the expression of c_2. Then by solving the quadratic equation (3.11), the factor κ can be determined to be

$$\kappa = \frac{c_2 + \sqrt{4 + c_2^2 + 4c_3 - 4c_1(1 + c_3)}}{2(1 - c_1)}|OP|. \tag{3.17}$$

Here we have excluded the negative root of Eq. (3.11), since we need $\kappa > 0$ to ensure that the 4-momentum of the photon is a past-directed vector to employ the backward ray-tracing method. Moreover, using the stereographic projection, we can build a map from the celestial sphere to the screen of our camera. In addition, note that, the momentum vector can be also expressed in the coordinate bases, that is, $p^\mu = \frac{dx^\mu}{d\tau}$. Thus, compared with Eq. (3.10), one can have the values of q_μ for the given pixels on the screen of the camera. Then, combining with the coordinates of the camera, one can find sets of (x^μ, q_μ). Putting these sets as initial values, we can do the numerical geodesic evolutions using Eqs. (2.6) and (2.7), and then identify the photons that will not fall into the black hole.

A. Deformation of Kerr black hole shadow

From Appendix, we can see that in the effective metric, among the three parameters a, λ, and B, the latter two always show up together. More precisely, λ is always partnered with B^2 in the effective metric and the geodesic equations. Hence, we can define a dimensionless parameter Λ standing for the field strength as

$$\Lambda = \lambda B^2. \tag{3.18}$$

In addition, when performing the calculations of black hole shadow, we should guarantee the validness of the causality of the effective metric. In the case at hand, we should always make sure $G_{\theta\theta}, G_{\phi\phi} > 0$ outside the horizon and $G_{tt} < 0$ outside the ergoregion. Unfortunately, from the expressions of the components of the effective metric, we cannot find an analytical bound for Λ. Therefore, we numerically check these inequalities and find that at least in the range $-0.2 \le \Lambda \le 0$, the effective metric works well. Thus, in the following, we would like to focus our attention to the allowed range $-0.2 \le \Lambda \le 0$.

Before we get into the analysis of shadows, we would like to discuss how large the magnetic field is in the International System of Units (SI for short); if we say $-0.2 \le \Lambda \le 0$ in our convention $c = G = \epsilon_0 = M = 1$. From Eq. (2.3), we can find

$$\mu = \frac{3.7 \times 10^{68}}{M_{\rm BH}^2}, \tag{3.19}$$

after some dimensional analysis, where μ is the value of the coupling constant in our convention and $M_{\rm BH}$ is the value of the black hole mass in SI. For example, $\mu = 0.1$ corresponds to $M_{\rm BH} \simeq 6 \times 10^{34}$ kg $= 3 \times 10^4\ M_\odot$ with $M_\odot$ being the mass of sun. On the other hand, for the magnetic fields, Gauss units rather than SI is customarily used. Similarly, we can find

$$B = 6 \times 10^{-51}\ B_{GS} M_{\rm BH}, \tag{3.20}$$

where B is the value of magnetic field intensity in our convention, $M_{\rm BH}$ is the value in SI, and B_{GS} is the value of the magnetic field intensity in Gauss units. Then, we have

$$\Lambda = \lambda B^2 \simeq -B_{GS}^2 \times 10^{30}. \tag{3.21}$$

From this relation, we can see that $-0.2 \le \Lambda \le 0$ means the magnetic field intensity is approximately $0 \le B_{GS} \le 4.5 \times 10^{14}$ Gauss.

Now we are ready to explore the shadows of the Kerr black holes bathed in the uniform magnetic fields in various cases. First, let us focus on the variations of the shadows with respect to the spin a of the Kerr black hole with fixed Λ and θ_o, where θ_o is the inclination angle of the observer.

In Fig. 2, we set $\Lambda = -0.01$ and $\theta_o = \frac{\pi}{2}$, and let the spin of the Kerr black hole, a, go from 0.2 to 0.999. Obviously, when a is small, the deformation of the shadow is very small, and the shadow looks very similar to the corresponding original Kerr black hole shadow. As the spin a goes up, the

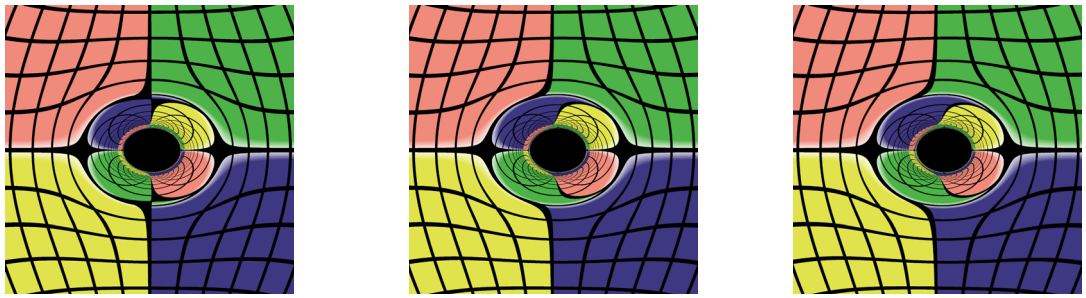

(a) $a = 0.2$ (b) $a = 0.5$ (c) $a = 0.7$

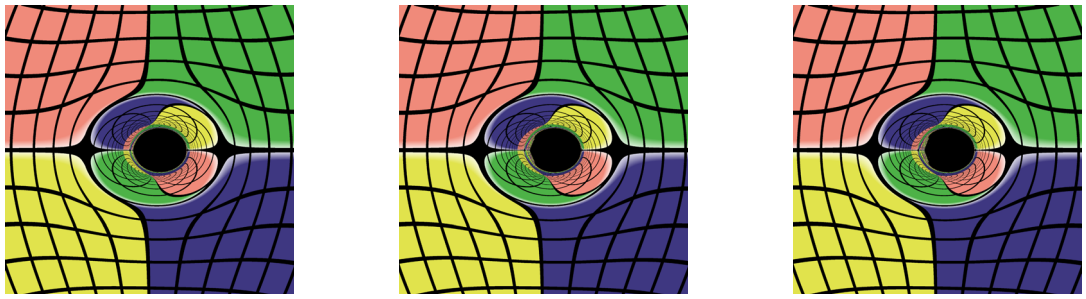

(d) $a = 0.9$ (e) $a = 0.99$ (f) $a = 0.999$

FIG. 2. The images of the Kerr black hole in uniform magnetic fields with parameter $\Lambda = -0.01$. The inclination angle of the observer is fixed at $\theta_o = \pi/2$.

left part of the shadow curve slowly shrinks, around the boundary and some photon "hairs" arise. In Fig. 3, we zoom into part of (f) with photon hairs in Fig. 2. In particular, when the spin is very near extremality, the photon hair becomes apparent. In addition, one can obviously find a region of discontinuity at the top-left corner of the shadow curve, and symmetrically a similar region in the right corner. These observations are significantly different with the shadow of the Kerr black hole without the magnetic field, in which the left boundary looks like a vertical line when the Kerr black hole is near extremality. These new features provide a potential way to verify whether the magnetic fields exist outside the horizon of a Kerr black hole if the EHT has enough capabilities to get a clear enough image of the black hole.

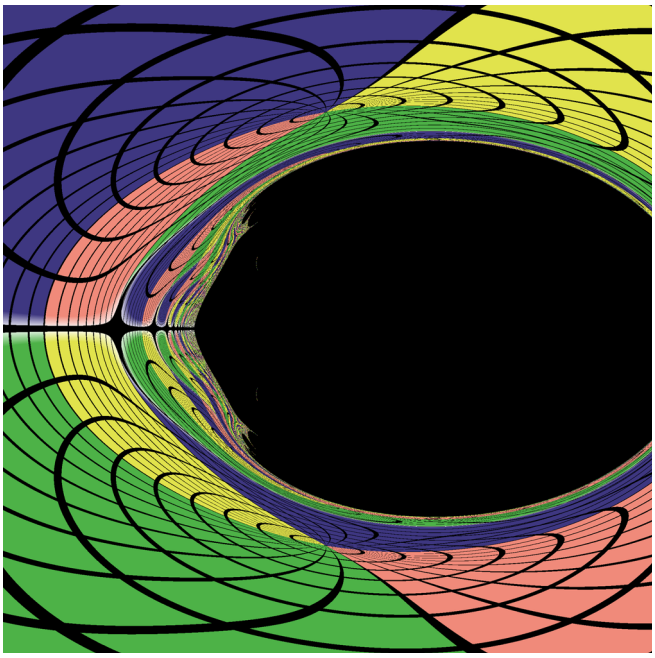

FIG. 3. The fine structure of the photon hairs of (f) in Fig. 2.

Next, let us move to the situation where the spin a and the observational angle θ_o are fixed at 0.5 and $\frac{\pi}{2}$, respectively. In Fig. 4, we can see the changes of the shadows as the parameter Λ vary from -0.01 to -0.20. The main feature is that the shadow curve is apparently stretched along the horizontal direction and squeezed along the vertical direction as the absolute value $|\Lambda|$ gets larger. In other words, when the strength of the magnetic field gets stronger, the Kerr black hole shadow becomes more flattened. This is reminiscent of the similar characteristic in the shadow of the Schwarzschild black hole bathed in a uniform magnetic field. In fact, when a is small, the frame dragging effect is negligible, so that many discussions on static black hole situations apply equally to the Kerr case—even though a little more complicated structures appear in the Kerr case—like the photon hairs in the neighborhood of the shadow curve.

Now, let us look at a near-extremal Kerr black hole with $a = 0.999$. We again fix the inclination angle of the observer at $\theta_o = \pi/2$ and let the parameter Λ go from -0.01 to -0.20. From Fig. 5, we can clearly see that the photon hairs

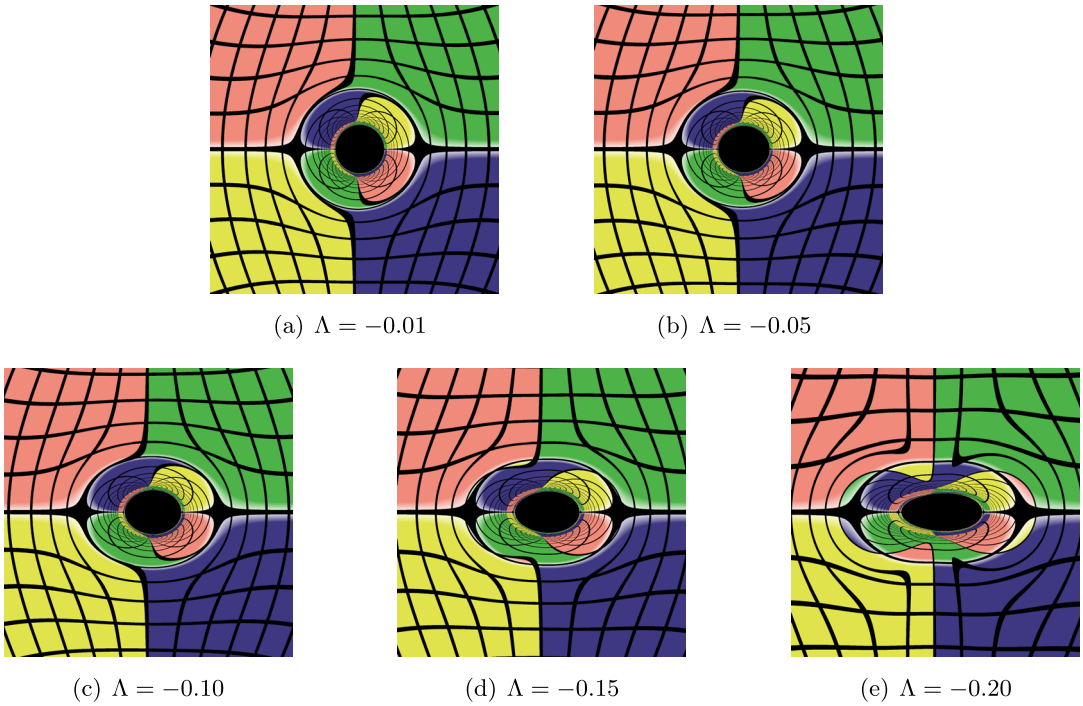

(a) $\Lambda = -0.01$ (b) $\Lambda = -0.05$

(c) $\Lambda = -0.10$ (d) $\Lambda = -0.15$ (e) $\Lambda = -0.20$

FIG. 4. The images of the Kerr black hole in uniform magnetic fields. The inclination angle of the observer is fixed at $\theta_o = \pi/2$ and the spin is fixed at $a = 0.5$.

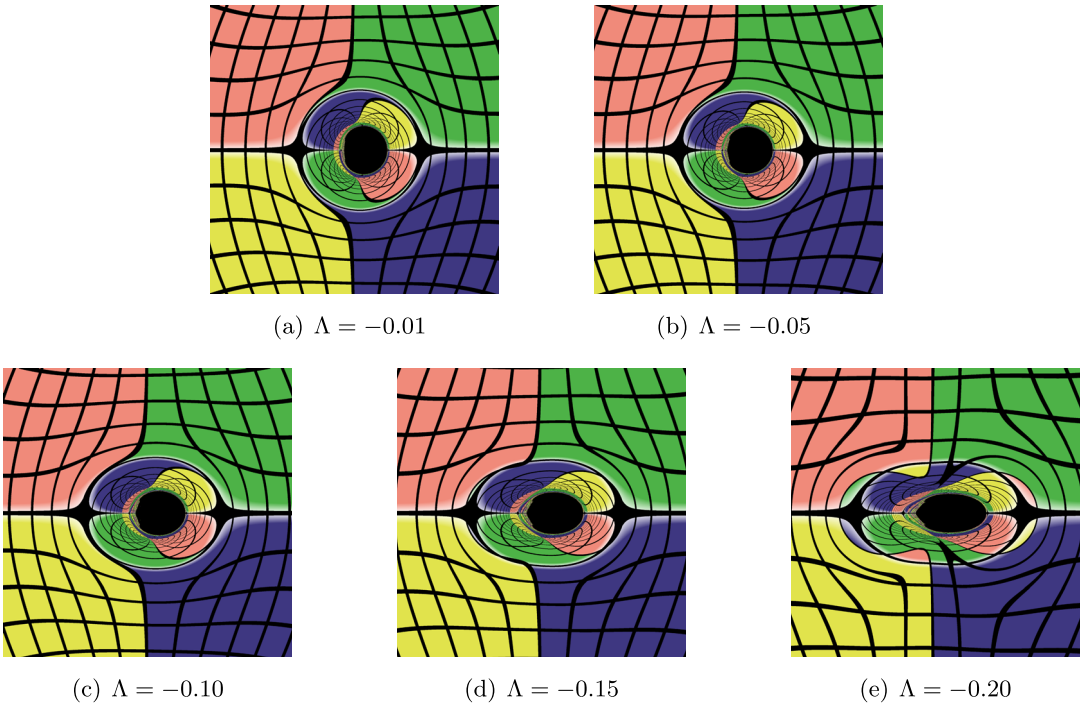

(a) $\Lambda = -0.01$ (b) $\Lambda = -0.05$

(c) $\Lambda = -0.10$ (d) $\Lambda = -0.15$ (e) $\Lambda = -0.20$

FIG. 5. The images of the Kerr black hole in uniform magnetic fields. The inclination angle of the observer is fixed at $\theta_o = \pi/2$ and the spin is fixed at $a = 0.999$.

become very obvious at $a = 0.999$ and, in addition to that, the shape of the shadow curve becomes more flattened as the parameter $|\Lambda|$ gets bigger. As shown in [8,11,12,45,46,51], for nonintegrable geodesic equations, the photons may travel in chaotic motions. In particular, in [45,46], the authors investigated the shadows of the black hole immersed in the Melvin magnetic field, and observed the chaotic motions of the photons. Furthermore, in [46], the authors found the

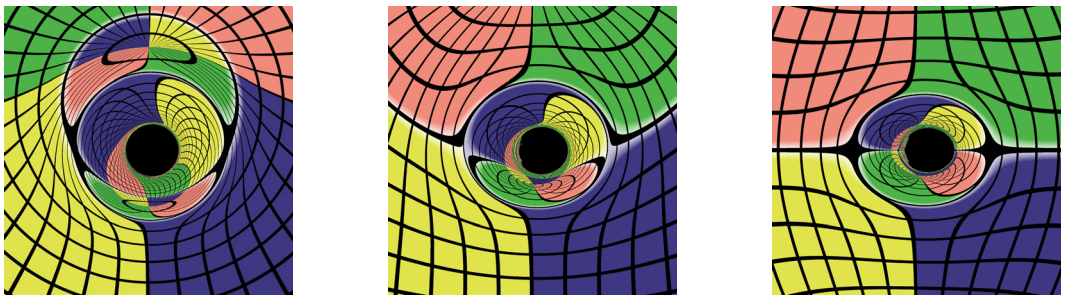

(a) $\theta_0 = 0.1\pi$ (b) $\theta_0 = 0.3\pi$ (c) $\theta_0 = 0.5\pi$

FIG. 6. The images of the Kerr black hole in uniform magnetic fields with $a = 0.999$ and $\Lambda = -0.1$.

photon hairs appearing at the left of the shadow curve as well, which is very similar to our findings. However the photon hairs found in our work have a bit more complicated structure; they extend two small hairs like a claw into the shadow region in a strange way, around the positions where the shadow curve is discontinuous. The appearance of the photon hairs is certainly an important feature that happens in a rotational black hole spacetime with a magnetic field, and different features in the photon hairs may help us to distinguish a uniform magnetic field from a Melvin magnetic field.

Moreover, it is also interesting to photograph the Kerr black hole from different inclination angles. Note that as the effective metric still has $\mathbb{Z}_2$ symmetry, we just have to consider $0 \leq \theta_o \leq \pi/2$. Three examples are shown in Fig. 6. We can see that the shadow is almost a perfect circle when θ_o is small, say 0.1π, because of the existence of a Killing vector field ∂_ϕ. As θ_o increases, it produces some irregular structures. In the picture (b), the upper small hair is separated and appears in the interior of the shadow. Finally, the irregular structure becomes symmetric along the horizontal line at $\theta_o = \pi/2$ due to the $\mathbb{Z}_2$ symmetry of the system.

B. Quantitative description of the deformation

In this subsection we would like to use characteristic parameters to quantify the deformation of the shadow of a Kerr black hole, due to a uniform magnetic field and its induced QED effect. Following [5,24], we introduce six parameters, $\{D_c, D_x, D_y, \bar{r}, \sigma_r, \sigma_{\text{Kerr}}\}$ to study the deviation driven by the QED effect quantitatively. To better interpret the meaning of these parameters, we present a diagram in Fig. 7, in which we place the shadow curve in the Cartesian coordinates (x, y) with the origin being the crosspoint of the boundary of four parts with different colors in the celestial sphere—x_{min} and x_{max} are the smallest and the largest values that can be taken from the points of the shadow's edge on the horizontal axis. Similarly, we get y_{min} and y_{max}, on the vertical axis. Note the $\mathbb{Z}_2$ symmetry of the effective metric, we have $y_{\text{min}} + y_{\text{max}} = 0$ for the cameras sitting on the equatorial plane.

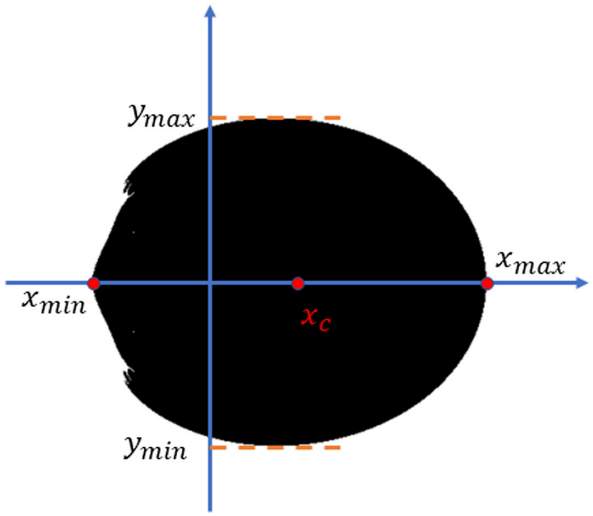

FIG. 7. A diagram of the Kerr black hole shadow curve, deformed by the QED effect from a uniform magnetic field around a black hole. The camera is located on the equatorial plane.

Then, we can easily introduce the definitions of other parameters. The center of the shadow is defined as

$$x_c \equiv \frac{x_{\text{max}} + x_{\text{min}}}{2} \tag{3.22}$$

on the horizontal axis. And y_c is defined similarly which is exactly zero due to the Z_2 symmetry. Thus the first parameter $D_c \equiv |x_c|$ measures the distance from the center of the shadow to the coordinate origin. And $D_x \equiv x_{\text{max}} - x_{\text{min}}$ and $D_y \equiv y_{\text{max}} - y_{\text{min}}$ are the width and the height of the shadow respectively.

From another perspective, we can define the polar coordinates (r, θ) with the origin at the center of the shadow, which means $r = [(x - x_c)^2 + y^2]$. Then the average radius is defined as

$$\bar{r} \equiv \int_0^{2\pi} r(\theta) d\theta / 2\pi, \tag{3.23}$$

TABLE I. Quantitative parameters characterizing shadows, with $a = 0.999$ and $\theta_0 = \pi/2$.

Parameters	Λ	D_c	D_x	D_y	$\bar{r}$	σ_r	$\sigma_r/\bar{r}$	σ_K
Values	−0.01	82.5	306	342	163.6	8.69	0.0531	0.0075
	−0.03	83.5	314	336	163.8	6.95	0.0424	0.0210
	−0.05	84.5	322	330	164.2	5.35	0.0326	0.0368
	−0.07	86.0	333	324	164.8	4.85	0.0294	0.0546
	−0.09	87.0	345	316	165.7	5.89	0.0355	0.0756
	−0.11	89.5	360	310	166.9	8.69	0.0521	0.0992
	−0.13	91.5	378	304	168.5	12.42	0.0737	0.1282
	−0.15	94.5	400	296	170.7	17.20	0.1007	0.1631
	−0.16	96.5	414	292	172.1	20.06	0.1166	0.1838
	−0.17	99.0	431	288	173.6	23.97	0.1380	0.2098
	−0.18	102.0	449	284	175.5	27.06	0.1542	0.2340
	−0.19	105.0	471	280	177.6	31.47	0.1772	0.2659
	−0.20	109.5	498	274	180.0	20.06	0.2039	0.3033

and the deviation from the sphericity is defined to be

$$\sigma_r \equiv \left\{ \int_0^{2\pi} [r(\theta) - \bar{r}]^2 d\theta / 2\pi \right\}^{1/2}. \tag{3.24}$$

At last, the deviation from a comparable Kerr BH ($\Lambda = 0$) is

$$\sigma_K \equiv \sqrt{\frac{1}{2\pi} \int_0^{2\pi} \left(\frac{r(\theta) - r_{\text{Kerr}}(\theta)}{r_{\text{Kerr}}(\theta)} \right)^2 d\theta}. \tag{3.25}$$

In Table I, we show these parameters describing the shadow when the spin $a = 0.999$ and the observational angle $\theta_0 = \pi/2$. In Fig. (8) we illustrate the variations of

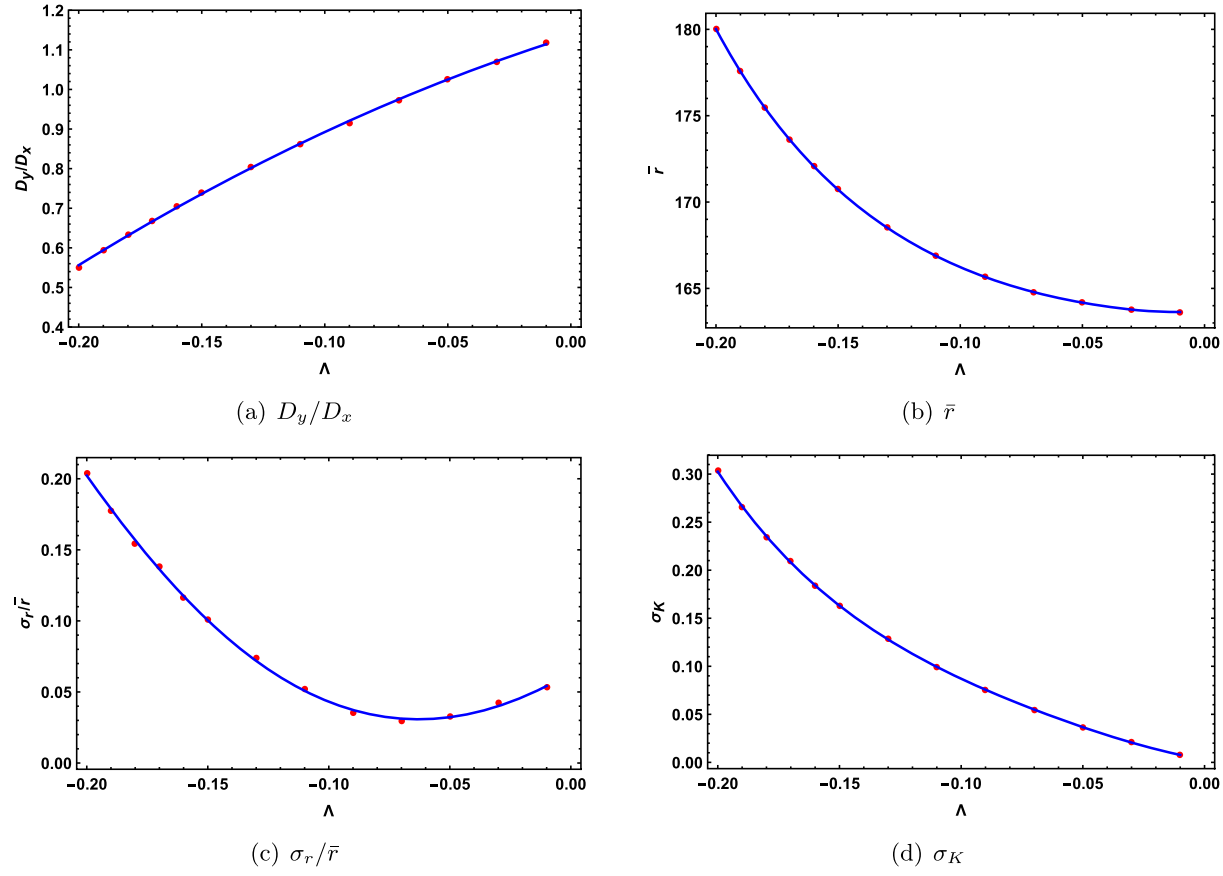

(a) D_y/D_x (b) $\bar{r}$

(c) $\sigma_r/\bar{r}$ (d) σ_K

FIG. 8. The variations of different parameters with respect to Λ. Here we fix $a = 0.999$ and $\theta_0 = \pi/2$.

D_y/D_x, $\bar{r}$, $\sigma/\bar{r}$ and σ_K with respect to Λ. Apparently, a stronger magnetic field leads to the increase of D_x and the decrease of D_y, which can be seen easily in Table I. Thus, in Fig. 8, we can see that the quantity D_y/D_x, which can somehow be regarded as oblateness, is an increasing function for $-0.2 \leq \Lambda \leq -0.01$. A similar observation also appears in the static black hole case which has been discussed in detail in [47]. An interesting thing is that when $a \geq 0$, we find that the deviation D_c becomes larger as the strength of the magnetic field increases. However, we are not sure if this finding has some useful implications in astronomical observations.

In addition, from the data of the average radius and the deviation from the sphericity in Table I, we can see that both of them go up when $|\Lambda|$ goes from 0.01 to 0.20, which means that an increasing uniform magnetic field would enlarge the circumference of the shadow. However, from Table I, as well as Fig. 8, we find that the deviation from the sphericity σ_r and the deviation per average radius $\sigma_r/\bar{r}$ are not monotonic functions of Λ; instead, they start to go down and then go up when the strength of magnetic field grows from weak to strong.

Finally, let us turn to the deviation from a comparable Kerr BH ($\Lambda = 0$), that is, σ_K. Both from Table I and Fig. 8, the derivation is found to increase with the strength of uniform magnetic fields. Furthermore, the rate of increase of the deviation also gets larger and larger as the magnetic field increases. These facts reveal that, for the Kerr black holes immersed in a uniform magnetic field with considerable strength, the shape of the shadow would be significantly different from that of the vacuum case, due to the QED effect. This result provides a potential way to measure the magnetic field outside a real black hole in our Universe.

IV. SUMMARY

In this paper we studied the QED effects on the shadows of the Kerr black holes immersed in magnetic fields. This generalized our previous study on static black holes [47] to stationary rotating black holes. In the Kerr black hole case, the effective metric involving the QED effects of the photons become much more complicated (see Appendix). Thus, we only focused on the uniform magnetic fields outside a Kerr black hole in this work. We mainly investigated the influence of the uniform magnetic fields on the shadows of Kerr black holes by employing the numerical backward ray-tracing method. We introduced a new dimensionless parameter $\Lambda = \lambda B^2$ to characterize the strength of the magnetic field. To guarantee the causality of the effective metric, we confined the parameter Λ to $[-0.20, 0]$. And when $\Lambda = 0$, it would reduce to the vacuum Kerr black hole case.

First, we paid our attention to $\Lambda = -0.01$ with the observer being located on the equatorial plane. We found that the deformation of the shadows became significant when the spin a is big enough. In particular, as a goes up, the left part of the shadow edge would shrink with some photon hairs appearing around the left edge. Moreover, we found that when the spin a goes to extremality, the hair structure would be very evident. A similar hair structure was also found in [46], where the Kerr Black hole shadows in Melvin magnetic field had been studied. It seems to us that the appearance of the hair structure in the shadow could be a common feature for the black hole in a magnetic field. The photon hairs may be taken as the signatures of the magnetic fields outside the black holes. Remarkably, the structure of the photon hairs may encode more detailed information on the magnetic field.

Then, we moved on to the study of the influences of magnetic fields with various strengths on the shadow while keeping the observer unchanged and fixing the spin $a = 0.5$. An interesting feature is that the Kerr black hole shadow becomes more flattened as the strength of magnetic field increases. The similar behavior has been found for the static black hole case [47]. Next, we discussed the influences of the magnetic fields on the near extremal Kerr black hole with $a = 0.999$. In addition to the hair structure that we just mentioned, we noticed the chaotic motions of the photons, due to the nonintegrability of the null geodesics in the effective spacetime. Moreover, we examined the shadows photographed by nonequatorial observers and discussed the features.

Furthermore, in Sec. III B, we made a quantitative analysis of the deformation of the Kerr black hole shadow due to the QED effects, by introducing six characteristic parameters to describe the shadow. Some interesting quantitative results are presented in Table I and Fig. 8.

ACKNOWLEDGMENTS

We thank Peng-Cheng Li for his efforts at the initial state of this work. The work is in part supported by NSFC Grants No. 11735001 and No. 11847241.

APPENDIX: EXPLICIT EXPRESSIONS OF THE EFFECTIVE METRIC FUNCTIONS

$$G_{tt} = g_{tt} + \frac{a^2B^2\lambda[(a^2+r^2-2r)(\cos 2\theta+3)^2(a^2\cos 2\theta+a^2-2r^2)^2-8(r^3-a^2r)^2(\cos 4\theta-1)]}{16(a^2\cos^2\theta+r^2)^5}, \tag{A1}$$

$$G_{t\phi} = g_{t\phi} + \frac{aB^2\lambda}{16(a^2\cos^2\theta + r^2)^5}\left[16r(a^2 - r^2)(a^2\cos^2\theta + r^2)^2\left(\frac{8r^3(a^2 + r^2)}{(2a^2\cos^2\theta + 2r^2)^2} + a^2 + r^2 - 2r\right)\sin^2 2\theta\right.$$
$$+ (a^4(r-1)\cos 4\theta + 3a^4(r-1) + 4a^2(a^2r - a^2 + 2r^3 + r^2)\cos 2\theta + 4a^2(2r+1)r^2 + 8r^5)$$
$$\left.\cdot \sin^2\theta(a^2 + r^2 - 2r)(\cos 2\theta + 3)(a^2\cos 2\theta + a^2 - 2r^2)\right], \tag{A2}$$

$$G_{rr} = g_{rr} + \frac{B^2\lambda}{16}\left[\frac{a^2(\cos 2\theta + 3)^2(\frac{4r(a^2+r^2)}{(2r-r^2-a^2)(a^2\cos 2\theta + a^2 + 2r^2)} - 1)(a^2\cos 2\theta + a^2 - 2r^2)^2}{(a^2\cos^2\theta + r^2)^4}\right.$$
$$- (128a^2r\sin^2\theta(\cos 2\theta + 3)(a^4(r-1)\cos 4\theta + 3a^4(r-1) + 4a^2(a^2(r-1) + r^2(2r+1))\cos 2\theta$$
$$+ 4a^2(2r+1)r^2 + 8r^5)(a^2\cos 2\theta + a^2 - 2r^2) - 4(a^4(r-1)\sin 5\theta + a^2(3a^2r - 3a^2 + 8r^3 + 4r^2)\sin 3\theta$$
$$+ 2(a^4(r-1) + 2a^2(2r+1)r^2 + 8r^5)\sin\theta)^2(a^2\cos 2\theta + a^2 + 2(r-2)r))$$
$$\left.\cdot (a^2 + r^2 - 2r)^{-1}(a^2\cos 2\theta + a^2 + 2r^2)^{-5}\right], \tag{A3}$$

$$G_{r\theta} = g_{r\theta} + 2B^2\lambda\sin 2\theta(r-1)$$
$$- \frac{2B^2\lambda}{(a^2 + (r-2)r)(a^2\cos 2\theta + a^2 + 2r^2)^5}[16a^2r^2(a-r)(a+r)\sin^3\theta\cos\theta$$
$$\cdot (a^4(r-1)\cos 4\theta + 3a^4(r-1) + 4a^2(a^2r - a^2 + 2r^3 + r^2)\cos 2\theta + 4a^2(2r+1)r^2 + 8r^5)]$$
$$+ \frac{2B^2\lambda\sin 2\theta r}{(a^2 + r^2 - 2r)(a^2\cos 2\theta + a^2 + 2r^2)^5}[2(r+1)(a^2 + r^2 - 2r)(a^2\cos 2\theta + a^2 + 2r^2)^4$$
$$- 2(3a^4 + 6a^2r(2r-1) + (r-10)r^3)(a^2\cos 2\theta + a^2 + 2r^2)^3 + 64r^3(a^2 + r^2)(a^4 + 3r^4)$$
$$- 16r(-a^6(r-1) + a^4r^2(r+1) + a^2r^4(5r+3) + r^6(3r+11))(a^2\cos 2\theta + a^2 + 2r^2)$$
$$+ 4(-a^6 + 7a^4r^2 + a^2r^3(13r - 12) + r^5(5r+4))(a^2\cos 2\theta + a^2 + 2r^2)^2], \tag{A4}$$

$$G_{\theta\theta} = g_{\theta\theta} + B^2\lambda\sin^2 2\theta\left[\frac{a^2r^2(a^2 - r^2)^2(-\frac{4r(a^2+r^2)}{(a^2+(r-2)r)(a^2\cos 2\theta + a^2 + 2r^2)} - 1)}{(a^2\cos^2\theta + r^2)^4}\right.$$
$$+ \frac{\csc^2\theta(a^2\cos 2\theta + a^2 + 2(r-2)r)(\frac{8r^3(a^2+r^2)}{(a^2\cos 2\theta + a^2 + 2r^2)^2} + a^2 + (r-2)r)^2}{(a^2 + (r-2)r)(a^2\cos 2\theta + a^2 + 2r^2)}$$
$$\left.+ \frac{32(\frac{8a^2r^9 - 8a^6r^5}{a^2+(r-2)r} - a^2r^2(a-r)(a+r)(a^2\cos 2\theta + a^2 + 2r^2)^2)}{(a^2\cos 2\theta + a^2 + 2r^2)^5}\right], \tag{A5}$$

$$G_{\phi\phi} = g_{\phi\phi} + \frac{B^2\lambda}{16(a^2\cos^2\theta + r^2)^5}\left[16\sin^2 2\theta\left(\frac{8r^3(a^2 + r^2)}{(a^2\cos 2\theta + a^2 + 2r^2)^2} + a^2 + (r-2)r\right)^2(a^2\cos^2\theta + r^2)^4\right.$$
$$+ (a^2 + (r-2)r)\sin^4\theta(a^4(r-1)\cos 4\theta + 3a^4(r-1) + 4a^2(a^2r - a^2 + r^2 2r^3 + r^2)\cos 2\theta$$
$$\left.+ 4a^2(2r+1)r^2 + 8r^5)^2\right]. \tag{A6}$$

[1] B. P. Abbott *et al.* (LIGO Scientific, Virgo Collaborations), Observation of Gravitational Waves from a Binary Black Hole Merger, Phys. Rev. Lett. **116**, 061102 (2016).

[2] K. Akiyama *et al.* (Event Horizon Telescope Collaboration), First M87 event horizon telescope results. I. The shadow of the supermassive black hole, Astrophys. J. Lett. **875**, L1 (2019).

[3] J. L. Synge, The escape of photons from gravitationally intense stars, Mon. Not. R. Astron. Soc. **131**, 463 (1966).

[4] J. M. Bardeen, Timelike and null geodesics in the Kerr metric, in *Part of Proceedings, Ecole d'Eté de Physique Théorique: Les Astres Occlus: Les Houches, France, 1972* (1972), pp. 215–240.

[5] P. V. P. Cunha, C. A. R. Herdeiro, E. Radu, and H. F. Runarsson, Shadows of Kerr Black Holes with Scalar Hair, Phys. Rev. Lett. **115**, 211102 (2015).

[6] S.-W. Wei, Y.-C. Zou, Y.-X. Liu, and R. B. Mann, Curvature radius and Kerr black hole shadow, J. Cosmol. Astropart. Phys. 08 (2019) 030.

[7] P.-C. Li, M. Guo, and B. Chen, Shadow of a spinning black hole in an expanding Universe, Phys. Rev. D **101**, 084041 (2020).

[8] P. V. P. Cunha, J. Grover, C. Herdeiro, E. Radu, H. Runarsson, and A. Wittig, Chaotic lensing around boson stars and Kerr black holes with scalar hair, Phys. Rev. D **94**, 104023 (2016).

[9] M. Guo and P.-C. Li, Innermost stable circular orbit and shadow of the 4*D* Einstein–Gauss–Bonnet black hole, Eur. Phys. J. C **80**, 588 (2020).

[10] V. Perlick and O. Y. Tsupko, Calculating black hole shadows: Review of analytical studies, arXiv:2105.07101.

[11] M. Wang, S. Chen, and J. Jing, Chaos in the motion of a test scalar particle coupling to the Einstein tensor in Schwarzschild–Melvin black hole spacetime, Eur. Phys. J. C **77**, 208 (2017).

[12] M. Wang, S. Chen, and J. Jing, Chaotic shadow of a non-Kerr rotating compact object with quadrupole mass moment, Phys. Rev. D **98**, 104040 (2018).

[13] Y. Hou, M. Guo, and B. Chen, Revisiting the shadow of braneworld black holes, Phys. Rev. D **104**, 024001 (2021).

[14] B. KIczek and M. Rogatko, Axion-like dark matter clouds around rotating black holes, arXiv:2106.01565.

[15] V. Cardoso and P. Pani, Testing the nature of dark compact objects: A status report, Living Rev. Relativity **22**, 4 (2019).

[16] E. Contreras, J. Ovalle, and R. Casadio, Gravitational decoupling for axially symmetric systems and rotating black holes, Phys. Rev. D **103**, 044020 (2021).

[17] A. Chowdhuri and A. Bhattacharyya, Shadow analysis for rotating black holes in the presence of plasma for an expanding Universe, Phys. Rev. D **104**, 064039 (2021).

[18] S. E. Gralla, A. Lupsasca, and A. Strominger, Observational signature of high spin at the event horizon telescope, Mon. Not. R. Astron. Soc. **475**, 3829 (2018).

[19] M. Guo, N. A. Obers, and H. Yan, Observational signatures of near-extremal Kerr-like black holes in a modified gravity theory at the Event Horizon Telescope, Phys. Rev. D **98**, 084063 (2018).

[20] H. Yan, Influence of a plasma on the observational signature of a high-spin Kerr black hole, Phys. Rev. D **99**, 084050 (2019).

[21] M. Guo, S. Song, and H. Yan, Observational signature of a near-extremal Kerr-Sen black hole in the heterotic string theory, Phys. Rev. D **101**, 024055 (2020).

[22] S. E. Gralla, D. E. Holz, and R. M. Wald, Black hole shadows, photon rings, and lensing rings, Phys. Rev. D **100**, 024018 (2019).

[23] J. Peng, M. Guo, and X.-H. Feng, Observational signature and additional photon rings of asymmetric thin-shell wormhole, arXiv:2102.05488.

[24] T. Johannsen, Photon rings around kerr and kerr-like black holes, Astrophys. J. **777**, 170 (2013).

[25] M. Guo and S. Gao, Universal properties of light rings for stationary axisymmetric spacetimes, Phys. Rev. D **103**, 104031 (2021).

[26] X.-X. Zeng, H.-Q. Zhang, and H. Zhang, Shadows and photon spheres with spherical accretions in the four-dimensional Gauss–Bonnet black hole, Eur. Phys. J. C **80**, 872 (2020).

[27] X.-X. Zeng, G.-P. Li, and K.-J. He, The shadows and observational appearance of a noncommutative black hole surrounded by various profiles of accretions, arXiv:2106.14478.

[28] Q. Gan, P. Wang, H. Wu, and H. Yang, Photon spheres and spherical accretion image of a hairy black hole, Phys. Rev. D **104**, 024003 (2021).

[29] J. Peng, M. Guo, and X.-H. Feng, Influence of quantum correction on black hole shadows, photon rings, and lensing rings, Chin. Phys. C **45**, 085103 (2021).

[30] M. Zhang and M. Guo, Can shadows reflect phase structures of black holes?, Eur. Phys. J. C **80**, 790 (2020).

[31] X.-C. Cai and Y.-G. Miao, Can shadows connect black hole microstructures?, arXiv:2101.10780.

[32] S.-Z. Han, J. Jiang, M. Zhang, and W.-B. Liu, Photon sphere and phase transition of d-dimensional ($d \geq 5$) charged Gauss–Bonnet AdS black holes, Commun. Theor. Phys. **72**, 105402 (2020).

[33] X. Wang, P.-C. Li, C.-Y. Zhang, and M. Guo, Novel shadows from the asymmetric thin-shell wormhole, Phys. Lett. B **811**, 135930 (2020).

[34] M. Guo, P.-C. Li, and B. Chen, Photon emission near myers-perry black holes in the large dimension limit, Phys. Rev. D **101**, 024054 (2020).

[35] P.-C. Li, M. Guo, and B. Chen, High spin expansion for null geodesics, Classical Quantum Gravity **38**, 065008 (2021).

[36] H. Yan, M. Guo, and B. Chen, Observability of zero-angular-momentum sources near kerr black holes, arXiv:2104.07889.

[37] V. Cardoso, A. S. Miranda, E. Berti, H. Witek, and V. T. Zanchin, Geodesic stability, Lyapunov exponents and quasinormal modes, Phys. Rev. D **79**, 064016 (2009).

[38] R. A. Konoplya and R. D. B. Fontana, Quasinormal modes of black holes immersed in a strong magnetic field, Phys. Lett. B **659**, 375 (2008).

[39] H. Yang, Relating black hole shadow to quasinormal modes for rotating black holes, Phys. Rev. D **103**, 084010 (2021).

[40] P.-C. Li, T.-C. Lee, M. Guo, and B. Chen, EQNM/UFPO correspondence for Kerr-Newman black hole, Phys. Rev. D **104**, 084044 (2021).

[41] R. A. Konoplya, Particle motion around magnetized black holes: Preston-Poisson space-time, Phys. Rev. D **74**, 124015 (2006).

[42] R. A. Konoplya, Magnetized black hole as a gravitational lens, Phys. Lett. B **644**, 219 (2007).
[43] K. Akiyama *et al.* (Event Horizon Telescope Collaboration), First M87 event horizon telescope results. VII. Polarization of the ring, Astrophys. J. Lett. **910**, L12 (2021).
[44] K. Akiyama *et al.* (Event Horizon Telescope Collaboration), First M87 event horizon telescope results. VIII. Magnetic field structure near the event horizon, Astrophys. J. Lett. **910**, L13 (2021).
[45] H. C. D. Lima, Jr., P. V. P. Cunha, C. A. R. Herdeiro, and L. C. B. Crispino, Shadows and lensing of black holes immersed in strong magnetic fields, Phys. Rev. D **104**, 044018 (2021).
[46] M. Wang, S. Chen, and J. Jing, Kerr Black hole shadows in Melvin magnetic field, Phys. Rev. D **104**, 084021 (2021).
[47] Z. Hu, Z. Zhong, P.-C. Li, M. Guo, and B. Chen, QED effect on a black hole shadow, Phys. Rev. D **103**, 044057 (2021).
[48] V. A. De Lorenci, R. Klippert, M. Novello, and J. M. Salim, Light propagation in nonlinear electrodynamics, Phys. Lett. B **482**, 134 (2000).
[49] M. Novello, V. A. De Lorenci, J. M. Salim, and R. Klippert, Geometrical aspects of light propagation in nonlinear electrodynamics, Phys. Rev. D **61**, 045001 (2000).
[50] R. M. Wald, Black hole in a uniform magnetic field, Phys. Rev. D **10**, 1680 (1974).
[51] S. Chen, M. Wang, and J. Jing, Chaotic motion of particles in the accelerating and rotating black holes spacetime, J. High Energy Phys. 09 (2016) 082.